


**Nonlinear transmission of laser light through coronal plasma due to self-induced incoherence**A. V. Maximov,<sup>\*</sup> J. G. Shaw, and J. P. Palastro *Laboratory for Laser Energetics, University of Rochester, Rochester, New York 14623, USA*

(Received 2 August 2019; revised 11 October 2019; accepted 8 July 2020; published 14 August 2020)

The success of direct laser-driven inertial confinement fusion (ICF) relies critically on the efficient coupling of laser light to plasma. At ignition scale, the absolute stimulated Raman scattering (SRS) instability can severely inhibit this coupling by redirecting and strongly depleting laser light. This article describes a new dynamic saturation regime of the absolute SRS instability near one-quarter of the critical density. The saturation occurs when spatiotemporal ion-acoustic fluctuations in the plasma density detune the instability resonance. The dynamic saturation mitigates the strong depletion of laser light and enhances its transmission through the instability region, explaining the coupling of laser light to ICF targets at higher plasma densities.

DOI: [10.1103/PhysRevE.102.023205](https://doi.org/10.1103/PhysRevE.102.023205)**I. INTRODUCTION**

While still in the research stage, controlled fusion could deliver an almost endless supply of power with relatively low environmental impact and a nearly inexhaustible reserve of fuel. As evidenced by active research programs throughout the world, the realization of such a technology would have lasting impact both geopolitically and for the health of our planet. In the direct-drive inertial confinement fusion (ICF) approach, an ensemble of laser beams symmetrically illuminates a cryogenic target containing thermonuclear fuel [1]. The illumination ionizes and heats the outer shell of the target, creating a pressure that drives inward fuel compression and outward mass ejection. The mass ejection creates a region of low-density plasma, or corona, that plays a critical role in direct-drive ICF: coupling of laser light to the corona determines the strength of the ablation pressure and, ultimately, the implosion performance [1,2].

Achieving efficient coupling of laser energy to the fusion target is arguably the most essential component of direct-drive ICF. A high ablation pressure requires the transmission of laser light to deep within the corona where collisions can efficiently convert electromagnetic energy to plasma thermal energy. To get there, however, the laser light must propagate through the outer corona, where it can drive a number of parametric instabilities [3,4]. In their nonlinear stage, these instabilities can redirect the incident light into unwanted directions and repartition the light energy into plasma waves. These waves can subsequently undergo local collisional damping, in which case the energy is deposited too far from the ablation surface, or collisionless damping, which creates nonthermal electrons that can preheat the fuel and reduce its compressibility [1,5]. In either case, the premature depletion of laser energy in this region presents a significant challenge for direct-drive ICF.

Within the United States, the primary direct-drive program has been centered around the Omega laser at the University

of Rochester, Laboratory for Laser Energetics. Compared to the National Ignition Facility (NIF), the high repetition rate of Omega serves as an ideal platform for studying the underlying physics of direct-drive. However, due to its limited laser pulse energy ( $\sim 30$  kJ), the Omega laser cannot create the conditions required for a burning fusion plasma. Consequently, the focus has turned to direct-drive implosions on the NIF. With its larger laser energy ( $> 1$  MJ), NIF can drive larger capsules, which changes characteristics of the plasma, e.g., the corona has a longer scalelength and higher electron temperature. As a result, absolute SRS becomes the dominant instability [6] in contrast to Omega experiments in which two-plasmon decay (TPD) dominates [4].

In SRS, an incident laser light wave decays into a scattered Raman light wave and an electron plasma wave [3,6–11]. In a region near the quarter of the critical plasma density  $n_c = m_e \omega_0^2 / 4\pi e^2$ , determined by the frequency of the laser  $\omega_0$ , the SRS decay waves can grow exponentially in time as an absolute instability until they nonlinearly saturate [7,8]. Recent planar-target experiments on the NIF that emulated the plasma corona of an ignition-scale direct-drive implosion showed a clear SRS feature originating from close to quarter-critical density and no clear evidence of TPD [6]. The observations confirmed theoretical estimates that, because of large density scalelengths in the plasma corona ( $\sim$  few hundred microns), the threshold for absolute SRS would be exceeded. Those same estimates also suggest that the instability would strongly deplete the laser light, preventing large transmission deep into the corona. Hydrodynamic evolution of NIF targets in planar [6] and polar-direct-drive [12] geometries was consistent with two-dimensional (2D) hydrodynamic modeling by code DRACO with the conversion of laser energy into plasma thermal energy without large pump depletion near quarter-critical density. As a result, a conceptual question emerges: What is a robust saturation mechanism for the absolute instability near quarter-critical density that would lead to high transmission of laser light through the instability region?

This article describes a dynamic saturation regime of the absolute SRS instability due to self-induced incoherence near quarter-critical density for conditions relevant to NIF scale

\*maximov.ur@gmail.com

TABLE I. Ignition-relevant NIF parameters used in the *LPSE* simulations.

Laser wavelength ( $\lambda_0$ )	0.351 $\mu\text{m}$
Scalelength ( $L$ )	500 $\mu\text{m}$
Electron temperature ( $T_e$ )	4 keV
Ion temperature ( $T_i$ )	2 keV
Ion charge ( $Z$ )	3.5
Ion atomic number ( $A$ )	2 $Z$
Density range	(0.21 to 0.265) $n_c$

implosions. As the incident light propagates through the instability region, it drives a primary SRS decay that initially depletes the laser intensity. The electron plasma waves resulting from the SRS decay then undergo a secondary instability that drives a broad spectrum of low-frequency density perturbations similar to the phenomenon described by DuBois *et al.* at lower densities [13]. The instability saturates when the density perturbations reach a high enough level to detune the primary SRS resonance, establishing a dynamic balance between the transmitted and scattered laser light. This dynamic, incoherent saturation mitigates depletion and facilitates the transmission of the laser light through the instability region, explaining how light can penetrate deep into the corona to efficiently drive ICF implosions.

Depending on plasma parameters, the saturation of SRS has been predicted to take several forms, such as the Langmuir decay instability (LDI) (when an electron plasma wave decays into another electron plasma wave and an ion-acoustic wave) [13–18], particle trapping [19–23], or SRS rescattering [24]. These saturation mechanisms were either studied in one spatial dimension [13,15,16] or in the kinetic modeling of SRS in low density plasma [19–24] that also considered the possibility of kinetic transition from convective to absolute SRS [25]. Previous 2D kinetic modeling of absolute SRS near quarter-critical density showed saturation through density profile steepening [26,27] or cavitation [28,29] for laser coupling strengths  $I_0\lambda_0^2 = (10^{15} - 10^{16}) \text{ W}\mu\text{m}^2/\text{cm}^2$  and density scalelengths  $< 100 \mu\text{m}$  (where  $I_0$  is the incident laser intensity and  $\lambda_0 = 2\pi c/\omega_0$  the laser wavelength). For NIF implosions, the intensities are much lower and the scalelengths are much longer (see Table I), so  $I_0\lambda_0^2 < 10^{14} \text{ W}\mu\text{m}^2/\text{cm}^2$ . Furthermore, in contrast to SRS in low density plasma, absolute SRS near quarter-critical density produces a plasma wave with a relatively small wave number ( $k_e\lambda_{De} \approx 0.15$ , where  $k_e \approx (2\pi/\lambda_0)\sqrt{1 - n_e/n_c}$ ,  $\lambda_{De} = \sqrt{T_e/4\pi e^2 n_e}$ ,  $n_e$  is the local electron density, and  $T_e$  the electron temperature). As a result, the linear Landau damping is very small ( $< 1 \text{ ns}^{-1}$ ) and the electron plasma waves dissipate primarily through collisional absorption ( $\sim 1 \text{ ps}^{-1}$ ), well before kinetic effects can play a role. For these values of  $k_e\lambda_{De}$ , one can recall the work of Sanbonmatsu *et al.* [30,31] that compared the amplitudes of plasma waves in fluid and kinetic models for the laser pump strength,  $\alpha = I_0/2cn_eT_e$ , being either “strong” ( $\alpha = 0.009$ ) [30] or “weak” ( $\alpha = 0.0028$ ) [31]. In our simulations  $\alpha < 0.003$ , and therefore the statement from Ref. [30] that ‘kinetic effects did not affect the saturation at the lower, “weakly driven” pump strength’ supports the validity of fluid model for the plasma parameters in our article.

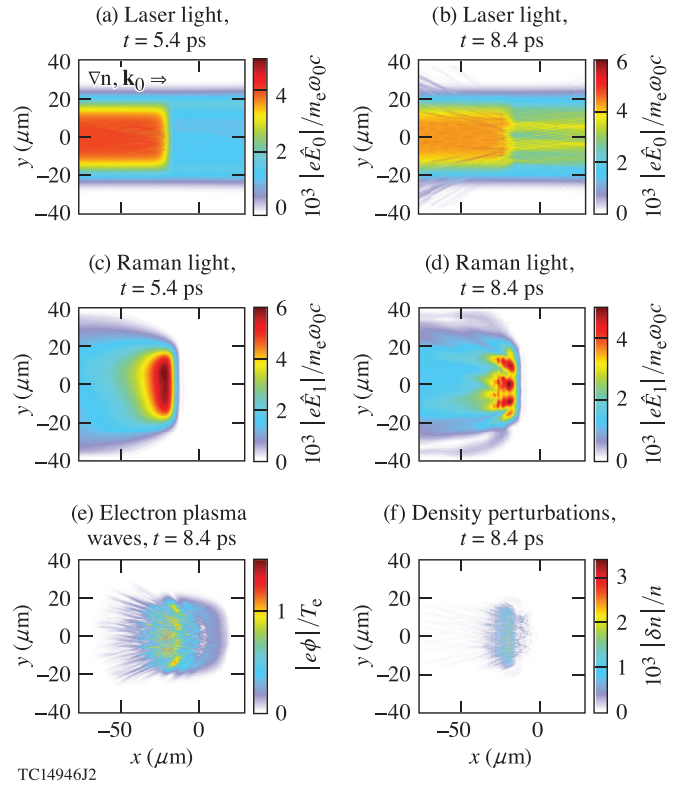


FIG. 1. The amplitudes of laser and Raman light waves at 5.4 ps [(a) and (c), respectively] and 8.4 ps [(b) and (d), respectively]. The amplitudes of (e) plasma waves (in terms of wave potential energy normalized to temperature) and (f) low-frequency density perturbations at 8.4 ps. The vacuum laser wavelength is 0.351  $\mu\text{m}$ .

## II. MODEL OF THE INSTABILITY

To investigate the saturation of absolute SRS in the regime relevant to direct-drive implosions at NIF scale, the laser-plasma simulation environment (LPSE) [32–34] was employed. LPSE applies a fluid plasma model to describe the evolution of the four waves (light, Raman, electron plasma, and ion-acoustic) and the couplings between them (see the Appendix). The simulations were performed in two spatial dimensions ( $x$  and  $y$ ) with  $s$ -polarized light (the electric field vectors of both the pump and Raman light waves were perpendicular to the simulation plane). The laser light was normally incident on a plasma with linear gradient  $n = \frac{1}{4}n_c(1 + x/L)$ , where  $L$  is the scalelength at the quarter-critical density.

The parameters, which are characteristic of CH plasmas from DRACO simulations of NIF scale direct-drive implosions, are listed in Table I. The ion-acoustic damping was obtained by solving for the roots of the kinetic dispersion relation for these parameters: a Landau damping rate of  $\gamma_i = 0.1kc_s$  for a perturbation wave vector  $k$ , where  $c_s = \sqrt{(ZT_e + 3T_i)/m_i}$  is the ion-acoustic speed and  $m_i$  the ion mass. At these conditions, the threshold for TPD is more than three times higher than the threshold for absolute SRS [6].

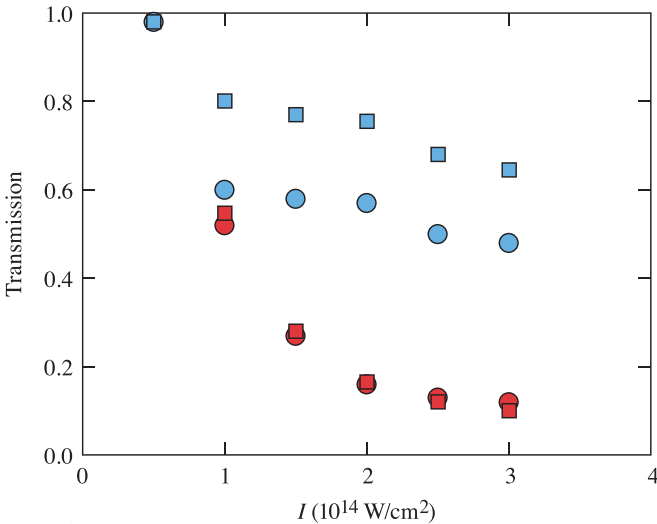
Figures 1(a) to 1(d) illustrate the nonlinear saturation of absolute SRS for laser light with an incident intensity of  $I_0 = 2 \times 10^{14} \text{ W}/\text{cm}^2$  (approximately three times greater than the theoretical instability threshold at these parameters,

$6 \times 10^{13} \text{ W/cm}^2$  [7]). Early in time, the laser light propagates through the plasma without scattering, but undergoes a small amount of collisional absorption,  $\sim 2\%$ . Shortly thereafter, the absolute instability develops. By 5.4 ps, the instability has strongly depleted the pump [Fig. 1(a)], and the Raman light [Fig. 1(c)] has grown to an amplitude comparable to the laser light. This pump depletion stage quickly gives way, 3 ps later, to a dynamic saturation stage in which the amplitudes of both the laser and Raman light become nonstationary and spatially incoherent [Figs. 1(b) and 1(d), respectively].

The development of spatial incoherence in the laser light can be understood as a two-step process: First, electron plasma waves amplified during absolute SRS [Fig. 1(e)] undergo a transverse scattering instability, which ponderomotively drives low-frequency ion fluctuations [Fig. 1(f)]. Second, resulting low-frequency fluctuations detune the SRS resonance and the dynamic saturation is established. These fluctuations also seed near-forward-stimulated Brillouin scattering (SBS) of the incident light wave, i.e., the decay of a light wave into a scattered light wave and ion-acoustic wave.

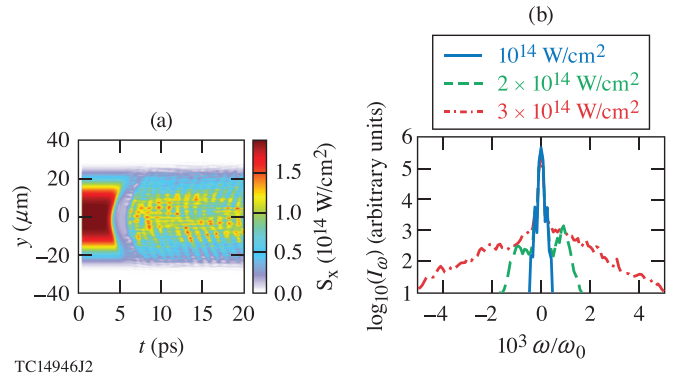
### III. TRANSMISSION OF LIGHT

The induced spatial incoherence increases the laser light transmission from  $T = 0.16$  in the pump depletion stage to  $T = 0.58$  in the dynamic saturation stage—a near four times increase in power transported deeper into the plasma corona. Figure 2 displays the scaling of the transmission, in both the pump depletion (red dark circles) and dynamic saturation (blue light circles) stages, as a function of laser intensity. At intensities below the absolute SRS threshold ( $I_0 < 6 \times 10^{13} \text{ W/cm}^2$ ), the transmission is reduced  $\sim 2\%$  due to inverse bremsstrahlung absorption. Above the threshold, the dynamic saturation increases the transmission well above the levels



TC14945J1

FIG. 2. The scaling of light transmission at the end of the pump depletion stage (red dark symbols) and during the dynamic saturation stage (blue light symbols) as a function of the incident laser intensity, for CH (circles) and Be (squares). Below threshold ( $I_0 < 6 \times 10^{13} \text{ W/cm}^2$ ) neither the SRS instability nor its dynamic saturation occur, so no red dark symbol is plotted.



TC14946J2

FIG. 3. (a) Transmitted Poynting flux as a function of time and transverse coordinate  $y$  for the laser intensity  $2 \times 10^{14} \text{ W/cm}^2$ , and (b) the frequency spectra of transmitted light for three incident laser intensities of  $10^{14} \text{ W/cm}^2$  (solid blue line),  $2 \times 10^{14} \text{ W/cm}^2$  (dashed green line), and  $3 \times 10^{14} \text{ W/cm}^2$  (dash-dotted red line).

determined by pump depletion alone. Reflection of the laser light accounts for only  $\sim 5\%$  of the drop in transmission.

Figures 1(c) to 1(e) show that the maximum plasma densities, at which the Raman scattered light and accompanying plasma waves are observed, are about  $0.243$  and  $0.257 n_c$ , respectively ( $\sim 3\%$  lower and higher than the quarter critical density at  $x = 0$ ). This is consistent with the frequency matching conditions for the primary SRS instability and previous 2D and three-dimensional (3D) particle-in-cell (PIC) simulations of plasmas with shorter density scalelengths ( $\sim 100 \mu\text{m}$ ) [35].

To study the dependence of the instability saturation and the resulting light transmission on the ion species, a set of simulations was performed for Be with  $Z = 4$  and  $A = 9$  and all other parameters the same as listed in Table I. The corresponding ion-acoustic damping was  $\gamma_i = 0.04k c_s$ . Figure 2 shows that the transmission in the pump-depletion stage is similar for Be and CH. However, in the dynamic saturation stage, the Be plasma has much higher transmission (blue light squares) because smaller ion-acoustic damping allows for larger ion-acoustic perturbations, which are more effective at detuning SRS.

The transmitted Poynting flux [Fig. 3(a)] and light spectra [Fig. 3(b)] demonstrate the presence of near-forward SBS. Figure 3(a) shows the longitudinal component of the transmitted Poynting flux exiting the simulation region as a function of time and transverse coordinate  $y$  for  $I_0 = 2 \times 10^{14} \text{ W/cm}^2$ . During the dynamic saturation stage (time  $> 7$  ps), the Poynting flux exhibits spatial incoherence with a scale of  $\ell \sim 2\lambda_0$  and temporal oscillations with a period  $\tau \sim 1$  ps. The two are connected by the ion-acoustic speed  $c_s \sim \ell/\tau$ , illustrating that the low-frequency ion-acoustic fluctuations spatiotemporally modulate the laser light.

Figure 3(b) displays the frequency spectra of the transmitted light, i.e., the Fourier transform of the temporal correlation function, calculated for three different incident intensities during the saturation stage (time  $> 7$  ps). The temporal incoherence, observable as the spectrum width, increases with intensity. At the lowest intensity (solid blue line),  $I_0 = 10^{14} \text{ W/cm}^2$ , the spectrum is narrowly peaked about the incident frequency. Stokes and anti-Stokes features appear at

an intensity of  $2 \times 10^{14}$  W/cm<sup>2</sup> (dashed green line). These sidebands have a spectral shift of  $\approx 10^{-3}\omega_0$ , corresponding to the 1-ps oscillations in the Poynting flux and the presence of near-forward SBS. At the largest intensity (dash-dotted red line),  $I_0 = 3 \times 10^{14}$  W/cm<sup>2</sup>, the spectrum has significantly broadened: large-amplitude SRS-generated plasma waves drive the transverse scattering instability to a nonlinear state, creating a broad spectrum of ion fluctuations that enhance the incoherence.

#### IV. WAVES INVOLVED IN THE INSTABILITY

Distinct features of the instabilities are clearly observed in the spatial spectra (i.e., Fourier transforms of the spatial correlation function) of the waves, illustrating the primary SRS decay, the transverse instability of the electron plasma waves, and near-forward SBS [Figs. 4(a) to 4(d)]. These figures display the spectra for the laser light, Raman light, electron plasma waves, and low-frequency density fluctuations, respectively. Foremost, the primary decay products of absolute SRS can be identified as the bright features near zero  $k$  for the Raman light [Fig. 4(b)] and near  $k_x \sim k_0$  and  $k_y = 0$  for the electron plasma waves [Fig. 4(c)]. Here  $k_0 = 2\pi/\lambda_0$  is the wave vector of the incident laser in vacuum.

The electron plasma waves generated from SRS undergo a decay instability in which their ponderomotive force drives ion-acoustic fluctuations in the direction transverse to the density gradient. The fluctuations then small-angle scatter the electron plasma waves, which, in turn, reinforces the transverse ponderomotive force. These phenomena can be observed in Figs. 4(c) and 4(d) as spreading in  $k_y$  about  $k_x \approx k_0$  for the electron plasma waves and about  $k_x \approx 0$  for the ion-acoustic waves. Figures 1(e) and 1(f) show the associated transverse ripples in the electrostatic potential of the electron plasma waves and the density of ion-acoustic

waves, respectively. Both waves are colocalized with the SRS instability region. In Fig. 4(c), the streaking in  $k_x$  results from the change in the wave number of the electron plasma waves as they propagate along the density gradient.

The dispersion relation for the transverse plasma wave instability (with ion-acoustic wave vector  $k_y$ ) can be obtained from the equations for the secondary plasma waves and the ion-acoustic perturbations [3,14]. At its resonance, this dispersion equation has the form

$$(\gamma + \gamma_i) \cdot (\gamma + \gamma_p) = \frac{\omega_e}{4} (k_y c_s) I_p, \quad (1)$$

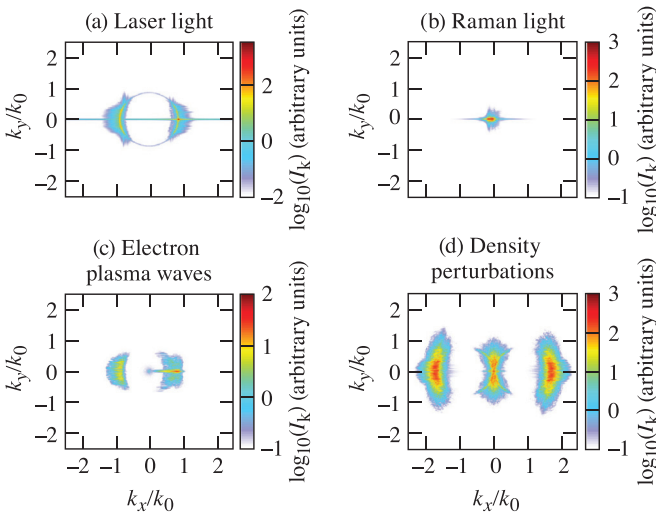
where  $\gamma$  is the growth rate,  $I_p = (|\hat{E}_e|^2/16\pi n_e T_e)$  is the normalized plasma wave intensity,  $\omega_e = \sqrt{4\pi e^2 n_e/m_e}$ , and  $\gamma_p$  is the damping rate for electron plasma waves. The instability threshold determined by Eq. (1) is readily exceeded during the growth stage of the primary SRS instability due to high plasma wave intensity. For a normalized plasma wave intensity  $I_p = 8 \times 10^{-3}$  and the transverse wave vector  $k_y \approx 0.15k_0$  observed in Fig. 4(d),  $\gamma \approx 2\text{ps}^{-1}$  consistent with Fig. 1(e).

The low-frequency density perturbations generated by the transverse instability seed small-angle SBS of the laser light. This manifests in Fig. 4(a) as the spreading in  $k_y$  about  $k_x \approx k_0$ . The spreading has an equivalent spatial scale of  $\sim 5\lambda_0$  and, through the ion-acoustic speed, a timescale of  $\sim 1$  ps consistent with Fig. 3(a).

The SRS-generated plasma waves can drive the LDI involving secondary plasma waves with the wave vector  $k_x \approx -k_0$  and the ion-acoustic waves with the wave vector  $\approx 2k_0$  [as seen in Figs. 4(c) and 4(d), respectively], and the backward LDI reduces the intensity of the SRS-generated plasma waves. At the same time, the secondary waves of the backward LDI are unlikely to detune the primary SRS because of their direction, whereas the transverse instability generates secondary waves that can detune the primary SRS resonance.

#### V. CONCLUSIONS

A novel regime for the saturation of the absolute SRS instability near the quarter-critical density has been shown to mitigate pump depletion and increase the transmission of laser light deep into the corona for parameters relevant to ignition-scale direct-drive implosions. The enhanced transmission explains why the temperature inferred in ignition scale experiments agrees with radiation hydrodynamics simulations that do not include a model for absolute SRS [6,12]. For example, if the intensity of light reaching the absorption surface was reduced by a factor of 2 due to pump depletion, radiation hydrodynamics simulations would predict a  $\sim 30\%$  lower electron temperature [36]. The dynamic saturation occurs when spatiotemporal fluctuations in the ion-acoustic density detune the SRS instability resonance. More specifically, the SRS-generated electron plasma waves undergo a transverse instability that drives a broad spectrum of ion-acoustic fluctuations. These fluctuations also seed near-forward Brillouin scattering of the laser light. The self-induced spatial incoherence answers a conceptual question in ICF: How does laser energy reach the inner corona when an absolute instability region stands in its way?



TC14947J2

FIG. 4. The spectra of (a) laser light waves, (b) Raman light waves, (c) plasma waves, and (d) low-frequency density perturbations in the dynamic saturation stage (at 8.4 ps) for the parameters of Fig. 1.

## ACKNOWLEDGMENTS

We acknowledge useful conversations with M. J. Rosenberg, R. K. Follett, A. A. Solodov, D. P. Turnbull, and D. H. Froula. This material is based upon work supported by the Department of Energy National Nuclear Security Administration under Award No. DE-NA0003856, the University of Rochester, and the New York State Energy Research and Development Authority. This report was prepared as an account of work sponsored by an agency of the U.S. Government. Neither the U.S. Government nor any agency thereof, nor any of their employees, makes any warranty, express or implied,

or assumes any legal liability or responsibility for the accuracy, completeness, or usefulness of any information, apparatus, product, or process disclosed, or represents that its use would not infringe privately owned rights. Reference herein to any specific commercial product, process, or service by trade name, trademark, manufacturer, or otherwise does not necessarily constitute or imply its endorsement, recommendation, or favoring by the U.S. Government or any agency thereof. The views and opinions of authors expressed herein do not necessarily state or reflect those of the U.S. Government or any agency thereof.

## APPENDIX

The LPSE model for the dynamic saturation of absolute SRS includes three time-enveloped wave equations for the electric fields of laser light  $\mathbf{E}_0 = \text{Re}[\hat{\mathbf{E}}_0(\mathbf{r}, t) \exp(-i\omega_0 t)]$ , Raman scattered light  $\mathbf{E}_1 = \text{Re}[\hat{\mathbf{E}}_1(\mathbf{r}, t) \exp(-i\omega_1 t)]$ , and electron plasma wave  $\mathbf{E}_e = \text{Re}[\hat{\mathbf{E}}_e(\mathbf{r}, t) \exp(-i\omega_e t)]$ , and a fourth, nonenveloped equation for the low-frequency density perturbation  $\delta n$ :

$$i \frac{\partial \hat{\mathbf{E}}_0}{\partial t} + i\gamma_0 \circ \hat{\mathbf{E}}_0 + \frac{c^2}{2\omega_0} [\nabla^2 \hat{\mathbf{E}}_0 - \nabla(\nabla \cdot \hat{\mathbf{E}}_0)] - \frac{\omega_p^2(\mathbf{r}) - \omega_0^2}{2\omega_0} \hat{\mathbf{E}}_0 = -\frac{e}{4\omega_1 m_e} (\nabla \cdot \hat{\mathbf{E}}_e) \hat{\mathbf{E}}_1, \quad (\text{A1})$$

$$i \frac{\partial \hat{\mathbf{E}}_1}{\partial t} + i\gamma_1 \circ \hat{\mathbf{E}}_1 + \frac{c^2}{2\omega_1} [\nabla^2 \hat{\mathbf{E}}_1 - \nabla(\nabla \cdot \hat{\mathbf{E}}_1)] - \frac{\omega_p^2(\mathbf{r}) - \omega_1^2}{2\omega_1} \hat{\mathbf{E}}_1 = -\frac{e}{4\omega_0 m_e} (\nabla \cdot \hat{\mathbf{E}}_e^*) \hat{\mathbf{E}}_0, \quad (\text{A2})$$

$$i \frac{\partial \hat{\mathbf{E}}_e}{\partial t} + i\gamma_e \circ \hat{\mathbf{E}}_e + \frac{3v_{Te}^2}{2\omega_e} \nabla^2 \hat{\mathbf{E}}_e - \frac{\omega_p^2(\mathbf{r}) - \omega_e^2}{2\omega_e} \hat{\mathbf{E}}_e = \frac{e\omega_e}{4m_e \omega_0 \omega_1} \nabla(\hat{\mathbf{E}}_0 \cdot \hat{\mathbf{E}}_1^*), \quad (\text{A3})$$

$$\frac{\partial^2 \delta n}{\partial t^2} + 2\gamma_i \circ \frac{\partial \delta n}{\partial t} - c_s^2 \nabla^2 \delta n = \frac{Z}{16\pi m_i} \nabla^2 \left[ |\hat{\mathbf{E}}_e|^2 + \frac{n_e}{n_c} \left( |\hat{\mathbf{E}}_0|^2 + \frac{\omega_0^2}{\omega_1^2} |\hat{\mathbf{E}}_1|^2 \right) \right], \quad (\text{A4})$$

where  $\omega_p = \sqrt{4\pi e^2(n + \delta n)/m_e}$  is the spatially dependent plasma frequency,  $v_{Te} = \sqrt{T_e/m_e}$  is the electron thermal velocity,  $\circ$  denotes a convolution, and  $\gamma_0$ ,  $\gamma_1$ , and  $\gamma_p$  are the damping rates for each wave. The carrier frequencies satisfy the Manley-Rowe relation  $\omega_0 = \omega_1 + \omega_e$ , with the density  $n_e$  selected within the range of the simulation, e.g., close to  $n_c/4$ . Inverse Bremsstrahlung damping was used for the damping rates of the pump and Raman light waves. The electron plasma waves were damped by both collisional damping, at a rate of  $1 \text{ ps}^{-1}$ , and Landau damping. The electron plasma waves were seeded at realistic thermal noise levels based on the Landau damping, but the absolute nature of SRS makes the results insensitive to the seed level. By retaining the second-order spatial derivatives in Eqs. (A1) to (A4), LPSE avoids making the paraxial approximation and can model waves propagating in arbitrary directions in inhomogeneous plasmas.

The simulations described by Figs. 1 to 4 were performed in the plasma region of  $116$  by  $80 \mu\text{m}$ , with the incident beam width of  $40 \mu\text{m}$ . Simulations with a wider plasma ( $116$  by  $116 \mu\text{m}$ ) and incident laser beam ( $80 \mu\text{m}$ ) exhibited similar instability evolution and dynamic saturation.

- 
- [1] R. S. Craxton, K. S. Anderson, T. R. Boehly, V. N. Goncharov, D. R. Harding, J. P. Knauer, R. L. McCrory, P. W. McKenty, D. D. Meyerhofer, J. F. Myatt *et al.*, *Phys. Plasmas* **22**, 110501 (2015).
- [2] V. N. Goncharov, T. C. Sangster, R. Betti, T. R. Boehly, M. J. Bonino, T. J. B. Collins, R. S. Craxton, J. A. Delettrez, D. H. Edgell, R. Epstein *et al.*, *Phys. Plasmas* **21**, 056315 (2014).
- [3] W. L. Kruer, *The Physics of Laser-Plasma Interactions* (Westview Press, Boulder, CO, 2003).
- [4] J. F. Myatt, J. Zhang, R. W. Short, A. V. Maximov, W. Seka, D. H. Froula, D. H. Edgell, D. T. Michel, I. V. Igumenshchev, D. E. Hinkel, P. Michel, and J. D. Moody, *Phys. Plasmas* **21**, 055501 (2014).
- [5] V. N. Goncharov, T. C. Sangster, P. B. Radha, R. Betti, T. R. Boehly, T. J. B. Collins, R. S. Craxton, J. A. Delettrez, R. Epstein, V. Yu. Glebov *et al.*, *Phys. Plasmas* **15**, 056310 (2008).
- [6] M. J. Rosenberg, A. A. Solodov, J. F. Myatt, W. Seka, P. Michel, M. Hohenberger, R. W. Short, R. Epstein, S. P. Regan, E. M. Campbell, T. Chapman, C. Goyon, J. E. Ralph, M. A. Barrios, J. D. Moody, and J. W. Bates, *Phys. Rev. Lett.* **120**, 055001 (2018).
- [7] J. F. Drake and Y. C. Lee, *Phys. Rev. Lett.* **31**, 1197 (1973).
- [8] C. S. Liu, M. N. Rosenbluth, and R. B. White, *Phys. Fluids* **17**, 1211 (1974).
- [9] J. L. Kline, D. S. Montgomery, B. Bezzerides, J. A. Cobble, D. F. DuBois, R. P. Johnson, H. A. Rose, L. Yin, and H. X. Vu, *Phys. Rev. Lett.* **94**, 175003 (2005).
- [10] D. J. Strozzi, D. S. Bailey, P. Michel, L. Divol, S. M. Sepke, G. D. Kerbel, C. A. Thomas, J. E. Ralph, J. D. Moody, and M. B. Schneider, *Phys. Rev. Lett.* **118**, 025002 (2017).
- [11] D. S. Montgomery, *Phys. Plasmas* **23**, 055601 (2016).
- [12] J. A. Marozas, M. Hohenberger, M. J. Rosenberg, D. Turnbull, T. J. B. Collins, P. B. Radha, P. W. McKenty, J. D. Zuegel, F. J. Marshall, S. P. Regan, T. C. Sangster, W. Seka, E. M. Campbell, V. N. Goncharov, M. W. Bowers, J.-M. G. Di Nicola, G. Erbert,

- B. J. MacGowan, L. J. Pelz, and S. T. Yang, *Phys. Rev. Lett.* **120**, 085001 (2018).
- [13] D. F. DuBois, H. A. Rose, and D. Russell, *Phys. Scripta* **T63**, 16 (1996).
- [14] D. F. DuBois and M. V. Goldman, *Phys. Rev.* **164**, 207 (1967).
- [15] J. A. Heikkinen and S. J. Karttunen, *Phys. Fluids* **29**, 1291 (1986).
- [16] T. Kolber, W. Rozmus, and V. T. Tikhonchuk, *Phys. Fluids B* **5**, 138 (1993).
- [17] S. Depierreux, C. Labaune, J. Fuchs, D. Pesme, V. T. Tikhonchuk, and H. A. Baldis, *Phys. Rev. Lett.* **89**, 045001 (2002).
- [18] J. P. Palastro, E. A. Williams, D. E. Hinkel, L. Divol, and D. J. Strozzi, *Phys. Plasmas* **16**, 092304 (2009).
- [19] H. X. Vu, D. F. DuBois, and B. Bezzerides, *Phys. Rev. Lett.* **86**, 4306 (2001).
- [20] H. X. Vu, L. Yin, D. F. Dubois, B. Bezzerides, and E. S. Dodd, *Phys. Rev. Lett.* **95**, 245003 (2005).
- [21] L. Yin, B. J. Albright, K. J. Bowers, W. Daughton, and H. A. Rose, *Phys. Rev. Lett.* **99**, 265004 (2007).
- [22] D. J. Strozzi, E. A. Williams, A. B. Langdon, and A. Bers, *Phys. Plasmas* **14**, 013104 (2007).
- [23] P. E. Masson-Laborde, W. Rozmus, Z. Peng, D. Pesme, S. Huller, M. Casanova, V. Yu. Bychenkov, T. Chapman, and P. Loiseau, *Phys. Plasmas* **17**, 092704 (2010).
- [24] B. J. Winjum, J. E. Fahlen, F. S. Tsung, and W. B. Mori, *Phys. Rev. Lett.* **110**, 165001 (2013).
- [25] Y. X. Wang, Q. Wang, C. Y. Zheng, Z. J. Liu, C. S. Liu, and X. T. He, *Phys. Plasmas* **25**, 100702 (2018).
- [26] A. B. Langdon, B. F. Lasinski, and W. L. Kruer, *Phys. Rev. Lett.* **43**, 133 (1979).
- [27] A. B. Langdon and B. F. Lasinski, *Phys. Fluids* **26**, 582 (1983).
- [28] C. Riconda, S. Weber, V. T. Tikhonchuk, and A. Heron, *Phys. Plasmas* **18**, 092701 (2011).
- [29] S. Weber, C. Riconda, O. Klimo, A. Heron, and V. T. Tikhonchuk, *Phys. Rev. E* **85**, 016403 (2012).
- [30] K. Y. Sanbonmatsu, H. X. Vu, B. Bezzerides, and D. F. DuBois, *Phys. Plasmas* **7**, 1723 (2000).
- [31] K. Y. Sanbonmatsu, H. X. Vu, D. F. DuBois, and B. Bezzerides, *Phys. Rev. Lett.* **82**, 932 (1999).
- [32] J. F. Myatt, R. K. Follett, J. G. Shaw, D. H. Edgell, D. H. Froula, I. V. Igumenshchev, and V. N. Goncharov, *Phys. Plasmas* **24**, 056308 (2017).
- [33] R. K. Follett, J. G. Shaw, J. F. Myatt, J. P. Palastro, R. W. Short, and D. H. Froula, *Phys. Rev. Lett.* **120**, 135005 (2018).
- [34] J. P. Palastro, J. G. Shaw, R. K. Follett, A. Colaitis, D. Turnbull, A. V. Maximov, V. N. Goncharov, and D. H. Froula, *Phys. Plasmas* **16**, 123104 (2018).
- [35] H. Wen, A. V. Maximov, R. Yan, J. Li, C. Ren, and F. S. Tsung, *Phys. Rev. E* **100**, 041201(R) (2019).
- [36] A. A. Solodov, private communication.